stellarator news

Published by Fusion Energy Division, Oak Ridge National Laboratory
Building 9201-2 P.O. Box 2009 Oak Ridge, TN 37831-8071, USA

Editor: James A. Rome Issue 86 March 2003
E-Mail: jar@ornl.gov Phone (865) 574-1306
On the Web at *http://www.ornl.gov/fed/stelnews*

Development of a robust class of quasi-poloidal compact stellarator configurations

Compact stellarators are toroidal confinement devices with low aspect ratio $A = \langle R \rangle / \langle a \rangle < 5$, a small number of toroidal field periods ($2 \leq N_p \leq 5$), and bootstrap current producing a small fraction of the magnetic rotational transform. They have been developed to combine the advantages of stellarators (in particular, steady-state operation and the avoidance of disruptions) and tokamaks (e.g., good particle and energy confinement at high beta) in an efficient and cost-effective plasma configuration. Specific examples are the National Compact Stellarator Experiment (NCSX), an $N_p = 3$ proof-of-principle device with $A = 4.4$, and the $A = 2.7$, $N_p = 2$ Quasi-Poloidal Stellarator (QPS), a concept exploration experiment. A QPS configuration is shown in Fig. 1.

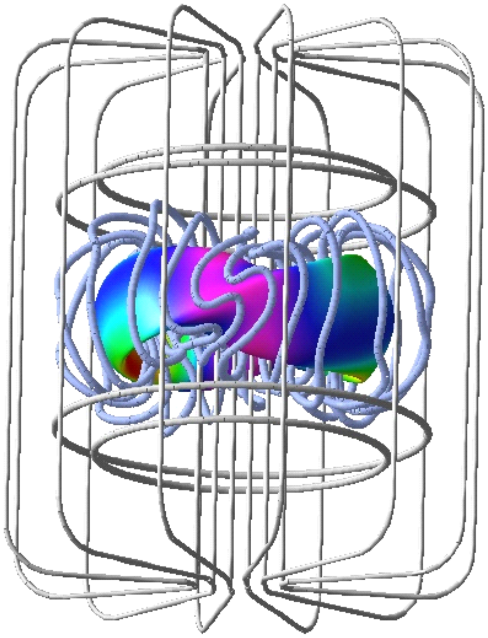

Fig. 1. An optimized QPS plasma and coil configuration.

Numerical optimization of three-dimensional (3D) plasmas [1], and the magnetic coil systems required to support them [2,3], has led to important advances in the design of high-aspect-ratio stellarators such as Wendelstein VII-X (W7-X) [4]. Recently, the stellarator optimization code STELLOPT [5] has been applied to low-aspect-ratio NCSX and QPS designs to determine the shape of the outer magnetic flux surface, together with internal plasma pressure and current profiles that produce desirable physics properties such as confined particle drift trajectories and plasma stability at significant beta.

In this issue . . .

The integration of the COILOPT [6] model, based on explicit representations for modular coils and coil geometry constraints, into the stellarator optimization package STELLOPT provides a unique and important computational tool for the design of compact stellarators. This self-consistent analysis ensures that physics and engineering criteria are simultaneously targeted in the full-pressure, full-current plasma/coil configuration. The analysis to date has been based on a local minimization method, a parallel version of the Levenberg-Marquardt algorithm [7], and is implemented after separate plasma and coil optimizations have identified a good starting point. This merged optimization technique has led to highly successful designs for the quasi-axisymmetric NCSX and the quasi-poloidally symmetric QPS.

The merged STELLOPT/COILOPT design approach [8] simultaneously optimizes plasma properties and coil engineering characteristics. For each evaluation of the physics and engineering targets, the equilibrium magnetic field is provided by the VMEC [9] code, which assumes the existence of nested, island-free magnetic flux surfaces. Following this analysis, two important stellarator design issues remain: (1) the question of the existence of good, nearly integrable, magnetic flux surfaces, and (2) the flexibility and robustness of the coil design with respect to variations of plasma profiles and coil currents. Original work by Cary and Hanson [10] to reduce islands in vacuum and more recent work by Hudson et al. [11] at nonzero beta offer a solution to the first of these problems. Island reduction is routinely applied to candidate NCSX coil configurations. Here we propose a method that addresses the second issue. It is based on including — in addition to the usual plasma confinement and stability properties at the full value of beta — a vacuum field condition that drives the combined optimization of the plasma and coil configuration into a region of parameter space with improved robustness and flexibility. We discuss the optimization of plasma and coils, the vacuum field target, and application of the technique to achieve an improved configuration for QPS.

Integrated optimization of plasma and coils

The compact stellarators and coils developed here were determined by a series of separate optimization steps. First a fixed-boundary plasma configuration independent of coils was determined using STELLOPT. This was followed by a COILOPT optimization to determine a candidate set of coils to approximately reproduce the desired plasma. These coils were subsequently refined by a combined plasma and coil optimization, using the merged STELLOPT/COILOPT code. The coils and plasma for the resulting compact stellarator are shown in Fig. 1. The coil set consists of nonplanar modular coils to provide the helical field, with toroidal field (TF) coils and vertical field (VF) coils for configurational flexibility. The coil design is subject to engineering constraints such as minimum coil-coil and coil-plasma separation and minimum coil radius of curvature.

In the STELLOPT code, the optimization is formulated as a least-squares minimization of a target $\chi^2 = \sum \chi_i(\boldsymbol{x})^2$, where the individual components χ_i are (generally nonlinear) functions of the system state-vector $\boldsymbol{x}$. Prior to merging with COILOPT, the state-vector $\boldsymbol{x}$ (independent variables) included coefficients describing the MHD plasma equilibrium pressure and current profiles, as well as either (1) Fourier coefficients of the plasma shape, in the case of a fixed-boundary optimization, or (2) coil currents, if the optimization is to be executed in free-boundary mode. The functions χ_i include both stellarator physics and coil engineering figures of merit that are evaluated numerically using a set of models dependent on the solution of a 3D plasma MHD equilibrium. Neoclassical transport, for example, is optimized using the NEO [12] code to evaluate a function χ_{NEO} returning values of the effective ripple factor ($\varepsilon_{\mathrm{eff}}^{3/2}$) on several magnetic flux surfaces.

Subroutines interface each physics and engineering model with the optimization code, and several models (e.g., NEO, COBRA [13], NESCOIL [2], TERPSICHORE [14]) are executed through system calls from these subroutines. Data from these models is passed to the optimization code through files, therefore requiring minimal modification to the software provided by the model developer. This is computationally efficient because the time required for evaluation of the physics model is typically long compared to the file-based data transfer time. Parallelization [15] on high-performance computers is simply implemented at the level of the optimization algorithm (e.g., computing the gradient of χ^2), not within individual physics and engineering models.

The COILOPT code is based on a parametric representation of coils confined to a coil-winding surface [6] (Fig. 2) $R = \Sigma_i R_i \cos[2\pi(m_i u + n_i v)]$, $Z = \Sigma_i Z_i \sin[2\pi(m_i u + n_i v)]$, $\phi = 2\pi(v/N_{\mathrm{p}})$, where u and v are the normalized poloidal and toroidal angles. The winding law for modular coils on this surface is described as a function of u and v by either Fourier series or a cubic spline representation $u(s) = \Sigma_j u_j B_j(s)$, $v(s) = \Sigma_j v_j B_j(s)$ (see Fig. 3). In the spline representation, the basis functions $B_j(s) = B_j(s; t_j, \ldots t_{j+4})$ are normalized cubic B-splines [16] defined on the interval [0,1] with a prescribed set of N+4 nondecreasing knots $t_j \in [0, 1]$. The N pairs of coefficients (u_j, v_j) are referred to as “control points” (Fig. 3) and are constrained to satisfy the appropriate periodic end conditions.

The winding law coefficients and the coil currents are all possible independent variables in the coil optimization problem. The spline representation allows control of local changes in coil geometry. The components of the objective function in COILOPT include residuals in the normal component of the magnetic field on the targeted plasma surface, together with engineering constraints on coil geometry.

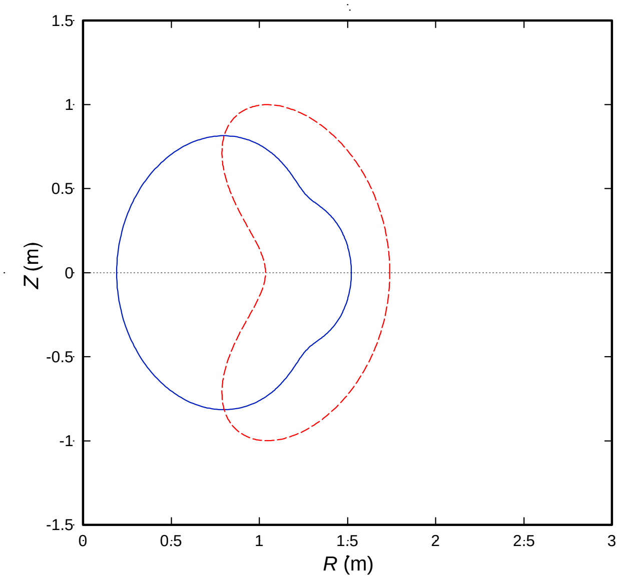

Fig. 2. The coil winding surface shown in the *v* = 0 (dashed) and *v* = 1/2 (solid) toroidal symmetry planes.

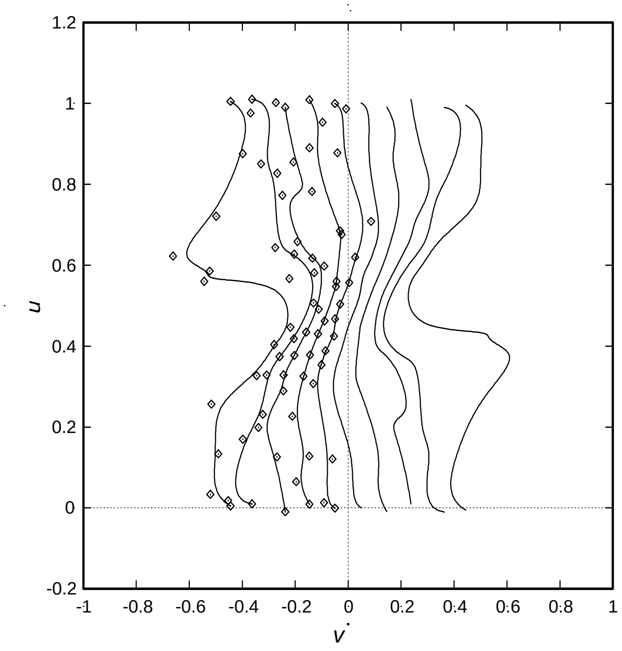

Fig. 3. The modular coil winding law, shown here for 10 of the 20 QPS winding packs, is determined by the location of cubic B-spline control points (associated with the 5 unique winding pack types) in *u*-*v* space.

In the merged plasma/coil optimization code, the state-vector $\boldsymbol{x}$ now consists of the independent variables from COILOPT (as described above), plus internal plasma profile coefficients from STELLOPT. Now, COILOPT is executed in a "single-step" mode from within STELLOPT to evaluate the coil-engineering penalty functions $\chi_i(\boldsymbol{x})$. A solution is achieved by targeting the physics parameters of the reference plasma and the geometric properties necessary for engineering coil design, while allowing the plasma boundary shape to vary in accordance with a free-boundary MHD equilibrium response to the external coils and currents.

Implementation of the robustness (vacuum field) constraint

Plasma flexibility and robustness are important components of stellarator coil design [17]. Of particular interest is the ability to obtain a vacuum field configuration having a large fraction of nearly integrable surfaces. The vacuum magnetic flux surfaces are typically evaluated by integration of the field line equations $\mathrm{d}R/\mathrm{d}\varphi = RB_R/B_\varphi$, $\mathrm{d}Z/\mathrm{d}\varphi = RB_Z/B_\varphi$ only *after* a coil configuration has been established by optimization at high beta. Thus, it has been heretofore difficult to directly influence this important vacuum equilibrium feature during the optimization process, which takes place at high beta.

In this work, a vacuum field term $\chi_B = \omega_B|\boldsymbol{B}\cdot\mathbf{n}|/|\boldsymbol{B}|$ is added to the STELLOPT objective function. Here, **n** is the normal to the *full-pressure* plasma boundary and $\boldsymbol{B}$ is the *vacuum* magnetic field due to the coils. During optimization, this term is minimized to force the last closed vacuum magnetic flux surface to enclose approximately the same volume as the full-pressure plasma. Evaluation of this function requires knowing the plasma boundary. Thus, COILOPT is called twice for each evaluation of the optimization objective function. The first call evaluates the coils needed to compute the free-boundary VMEC equilibrium. The next call then uses the computed plasma boundary to evaluate plasma-dependent constraints, including χ_B and the minimum plasma-coil distance.

Experience shows that to obtain a plasma volume bounded by good vacuum flux surfaces that is comparable to the high-beta equilibrium requires an average error

$$\langle\delta B\rangle = (1/A)\int_{\partial P}\mathrm{d}A|\boldsymbol{B}\cdot\mathbf{n}|/|\boldsymbol{B}| \le 1.3\%$$

for the normal component of the vacuum magnetic field at the full-pressure plasma boundary ∂P.

Design optimization for QPS

The QPS is a concept exploration experiment to investigate the effects of 3D shaping and quasi-poloidal symmetry ($\partial|\boldsymbol{B}|/\partial\theta \approx 0$, where θ is a poloidal angle) on neoclassical confinement at moderate beta in a very low aspect ratio ($A \le 2.7$) compact stellarator. The QPS plasma has two field periods, average major radius $\langle R\rangle =$

0.9 m, magnetic field $\langle B \rangle = 1$ T, and infinite-*n* ballooning stable limit $\langle \beta \rangle = 2\%$. The QPS coil set (Fig. 1) consists of 20 modular coil winding packs (described below), 12 TF coils capable of changing the toroidal field on axis by ± 0.2 T, and 2 pairs of circular VF coils. Additional engineering requirements for the QPS modular coils include a minimum space of 40 cm between the center lines of the coil winding packs across the center of the device for the TF legs and solenoid coils.

Every modular coil in QPS consists of two winding packs, each containing multiple turns of multistrand flexible copper conductor, separated by a central structural "web," and wound on a machined winding form. In the present study, each winding pack is modeled with a single central filament. An early innovation in the QPS design was to allow one of the four coil types (the coils nearest the center of the field period, or in the $v = 1/2$ symmetry plane) to have winding packs that follow independent (nonparallel) paths (Fig. 4). This design required that the structural web of the "split" coil vary in width along the trajectory of the coil. This provided the ability to create a more highly shaped magnetic field in the critical inboard region of the plasma near $v = 1/2$ without increasing either the total number of modular coils or the number of coil winding forms. Both of these are major cost drivers in compact stellarator coil design.

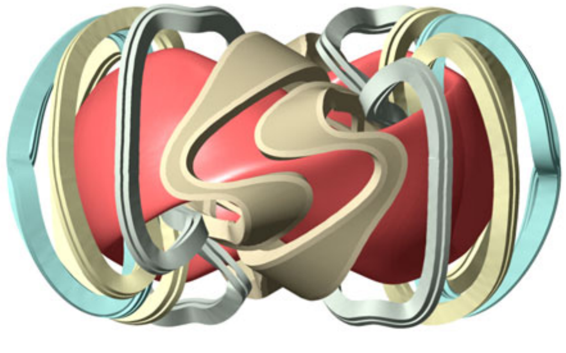

Fig. 4. The coil winding packs of the modular coils near the $v = 1/2$ symmetry plane in the QPS PAC reference configuration follow independent paths.

A recent change of the QPS coils was to allow *all* coils to have this variable web structure and to combine the winding packs *across* the $v = 1/2$ symmetry plane into a single coil. This implies that the winding packs near the $v = 0$ symmetry plane belong to different coils (of the same coil type), leaving a large space near the $v = 0$ plane for access to the plasma. The significance of this rearrangement is the reduction in the number of required winding form types from 4 to 3 (Fig. 5), the number of modular coils from 16 to 10, and the number of individual winding packs from 32 to 20. These changes lead to a significant reduction in the cost of the modular coils.

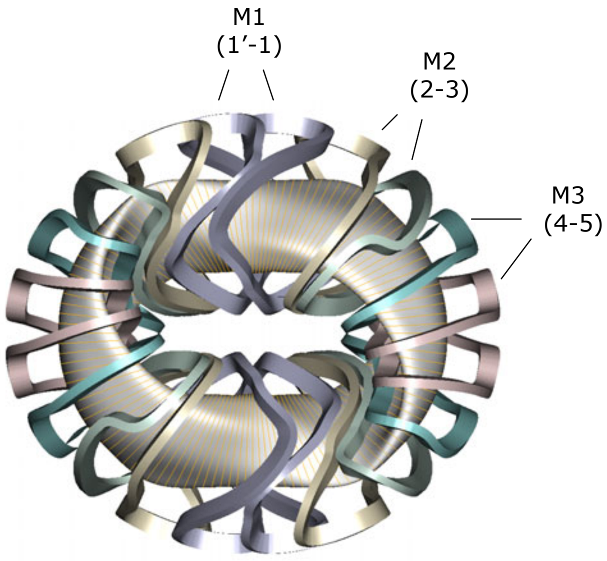

Fig. 5. Modular coils M1 (consisting of winding packs 1'-1), M2 (2-3), and M3 (4-5) are shown for the improved QPS configuration. Each pair of winding packs will be connected with a structural web that varies in width along the trajectory of the coil.

This new configuration was achieved by adding individual coil-coil spacing constraints in COILOPT. Previously, only a minimum distance $\Delta_n^{(\mathrm{min})}$ to all other coils was targeted for each of the four unique coil types. The new optimization targets a matrix of coil minimum separation constraints comparing each unique coil winding pack type *n* with a specific coil winding pack $m \neq n$, i.e.,
$\chi_{n,m} = \max\{0, \omega_{n,m}(\Delta_{n,m}^{(\mathrm{target})} - \Delta_{n,m}^{(\mathrm{min})})\}$.
Thus, windings that are considered part of the same coil can be assigned a smaller separation target distance than those that are not joined by a structural web. This allows more spacing between separate coil pairs and the flexibility to orient the individual winding packs to improve fabricability.

Table 1 compares, for filamentary coils, the reconfigured coil system (obtained using the vacuum field constraint), with the QPS design [18] presented at the December 2002 QPS Program Advisory Committee (PAC) meeting. For comparable aspect ratio, both plasma and coil characteristics have been improved in the present design. Plasma volume and ballooning-stable beta are increased, and neoclassical confinement in the $1/\nu$ regime, characterized here by the effective ripple at $r/a \sim 0.7$ (flux $s = 0.5$), is also improved; the ripple transport is decreased by a factor of 2.6. This is directly correlated with a reduction of neoclassical toroidal viscosity, so the present design should allow greater control of the ambipolar potential and associated poloidal rotation for reduction of anomalous transport.

Table 1. Comparison of an improved QPS plasma and coil optimization (022103a) with the reference configuration presented at the December, 2002 PAC meeting.

Target	PAC Reference	Improved Case
Aspect ratio, *A*	2.65	2.76
Volume (m^3)	1.81	2.27
Average elongation	3.26	3.68
Bootstrap current (kA)	45.9	37.8
Ballooning beta — infinite *n* (%)	1.83	2.00
Ripple diffusion ($s = 0.5$)	.00353	.00135
Iota at maximum beta		
$s = 0$	0.293	0.281
$s = 0.5$	0.341	0.324
$s = 1.0$	0,345	0.329
Normal vacuum field error (%, $s = 1$)		
Average	1.82	1.27
Maximum	6.45	4.34
Min. coil-plasma separation (cm)	13.0	15.4
Min. coil separation (cm)		
Filament 1'-1	14.9	9.4
Filament 1-2	6.1	13.0
Filament 2-3	9.6	10.4
Filament 3-4	11.0	13.1
Filament 4-5	13.8	13.9
Filament 5-5’	18.0	18.1
Min. radius of curvature (cm)		
Filament 1	9.3	12.8
Filament 2	9.4	12.3
Filament 3	11.0	12.2
Filament 4	12.4	15.3
Filament 5	14.2	16.4
Total coil length (m)	90.4	101.6
Max. coil *R* (m)	1.64	1.73
Min. distance across center, ΔY (cm)		
Winding pack 1	36.0	40.0
Winding pack 2	37.0	43.4
Winding pack 3	38.2	40.0

Vacuum magnetic surfaces for the new configuration are compared with those of the PAC design in Figs. 6 and 7 for the $v = 1/2$ symmetry plane. In the new configuration, the targeted vacuum normal field error has been significantly reduced at the location of the $s = 1$ full-beta boundary (see Table 1). The coil currents are the same as those for the full-beta case and not optimized for low beta. This leads to a plasma volume in vacuum that is comparable to, or larger than, that of the full-beta case and which exhibits a large fraction of closed magnetic surfaces (compared to islands). The average low-beta plasma radius can be >40 cm (vs 34 cm for the full-beta configuration). This preservation of aspect ratio with beta is important, since QPS experiments that focus on neoclassical transport reduction will be conducted at low beta. A small $n = 2$, $m = 9$ island chain is seen in Fig. 7. Island chains such as this may be targeted through the variation of coil currents (within the bounds set by power supply capability) and, if necessary, the addition of small correction coils. Magnetic islands do not seem to be an issue at higher beta. There is no low-order resonant surface in the plasma at full beta. A recent PIES calculation [19] shows only a small $n = 6$, $m = 19$ island chain in the plasma and an outer flux surface that is larger than the original VMEC surface. In addition, the equilibrium bootstrap current is lower in the new configuration despite the higher beta and larger plasma volume, so there is a smaller difference between the iota profiles at low and full beta.

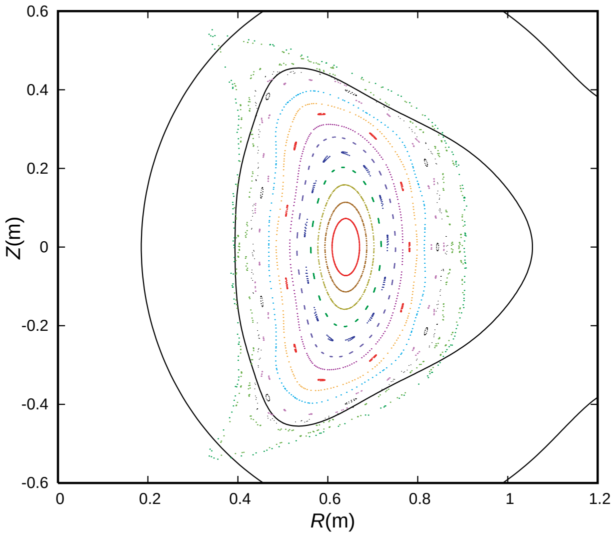

Fig. 6. Vacuum magnetic surfaces for the QPS PAC coil configuration shown in the $v = 1/2$ symmetry plane. The outer solid line is the coil winding surface and the inner solid line is the full-beta VMEC plasma boundary.

The coil engineering features of the new configuration are also significantly improved (Table 1). Minimum plasma-coil separation, important for allowing adequate plasma scrape-off distance and divertor operation, has increased by 2 cm (15%). The minimum distance across the central region of the torus ΔY, a critical parameter related to the design of TF coil inner legs and the central solenoid, is also larger by 4 cm. In the previous design, the twist of the modular coil cross sections had to be carefully modulated to avoid coil interferences in some regions. Increasing the minimum center line separation (to >12 cm) between winding packs belonging to different coils, and the minimum coil radius of curvature (to ~12.5 cm), has greatly improved the feasibility of the coil engineering design, allowing for both easier coil manufacture and larger experimental excursions in coil currents. Small increases in maximum coil radius and the total coil length are more than offset by these improvements in engineering feasibility and the cost reduction that occurs by decreasing the number of winding forms. All distances in Table 1 are to the center line of the filamentary coils. The relatively small dimensions of the coil winding packs reduce the coil spacing, but still leave more than adequate clearance in all cases.

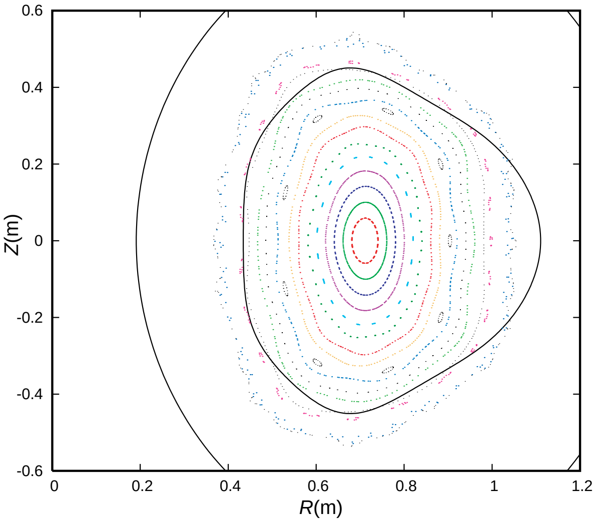

Fig. 7. Vacuum magnetic surfaces for the improved coil configuration 022103a shown in the $v = 1/2$ symmetry plane. The outer solid line is the coil winding surface and the inner solid line is the full-beta VMEC plasma boundary.

Summary

The capability for numerical optimization of high-beta compact stellarator plasma and coil configurations has been extended through the implementation of a vacuum field constraint in the STELLOPT/COILOPT plasma and coil optimization code. In addition to the existing measures of plasma stability and transport at a reference value of beta, and engineering design constraints on coil geometry, this new target minimizes the normal component of the vacuum magnetic field at the full-pressure plasma boundary. This minimization serves to guide the solution into a new region of parameter space where, in addition to good plasma and coil properties at the reference beta, the last closed vacuum magnetic flux surface encloses a large plasma volume that is similar in shape to the finite-beta volume. This vacuum field constraint, and recent changes in the coil model have resulted in an improved plasma and coil configuration for the QPS. The configuration shows some of the invariance to beta changes built into the W7-X design [4] while preserving the ability to sustain finite bootstrap currents.

D. J. Strickler, S. P. Hirshman, D. A. Spong, L. A. Berry,
M. J. Cole, J. F. Lyon, B. E. Nelson, A. S. Ware,
and D. E. Williamson
Oak Ridge National Laboratory
P. O. Box 2009, MS 8071
Oak Ridge, TN 37831-8071, USA
E-mail: stricklerdj@ornl.gov

References

[1] J. Nührenberg and R. Zille, Phys. Lett. A **114**, 129 (1986).

[2] P. Merkel, Nucl. Fusion **27,** 5, 867 (1987).

[3] M. Drevlak, Fusion Technol. **33,** 106 (1998).

[4] G. Grieger et al., in Proc. 13th Int. Conf. Plasma Physics and Nuclear Fusion Research, Washington, D.C., October 1–6, 1990, Vol. 3, p. 525, International Atomic Energy Agency (1991).

[5] D. A. Spong et al., Nucl. Fusion **41**, 711 (2001).

[6] D. J. Strickler, L. A. Berry, and S. P. Hirshman, Fusion Sci. Technol. **41**, 107 (2002).

[7] J. J. More, B. S. Garbow, and K. E. Hillstrom, "User's Guide to MINPAC-I," Argonne National Laboratory (1980).

[8] D. J. Strickler, L. A. Berry, S. P. Hirshman, et al., "Integrated Plasma and Coil Optimization for Compact Stellarators," presented at the 19th IAEA Fusion Energy Conference, Lyon, France (October 2002).

[9] S. P. Hirshman and J. C. Whitson, Phys. Fluids **26** (12) 3553 (1983).

[10] J. R. Cary and J. D. Hanson, Phys. Fluids **29** (8), 2464–2473 (1986).

[11] S. R. Hudson et al., Phys. Rev. Lett. **89**, article 275003 (2002).

[12] V. V. Nemov et al., Phys. Plasmas **6**, 4622 (1999).

[13] R. Sanchez et al., J. Comput. Phys. **161**, 576 (2000).

[14] D. V. Anderson et al., Int. J. Supercomput. Appl. **4**, 34 (1990).

[15] D. A. Spong, et al., "QPS Plasma and Coil Optimization," presented at the 13th International Stellarator Workshop, Canberra, Australia (February, 2002).

[16] C. de Boor, "A Practical Guide to Splines," Springer-Verlag (1978).

[17] N. Pomphrey et al., "Flexibility and Robustness Calculations for NCSX," Princeton Plasma Physics Laboratory Report PPPL-3701 (June 2002).

[18] J. F. Lyon et al., "Physics Issues for a Very-Low-Aspect-Ratio Quasi-Poloidal Stellarator (QPS),"presented at the 19th IAEA Fusion Energy Conference, Lyon, France (October 2002), to be published.

[19] D. Monticello, private communication.

Increase of ion temperatures in NBI discharges with argon gas puffing and impurity pellet injection in LHD

Extensive ion heating experiments have been carried out during discharges with electron cyclotron heating (ECH), ion cyclotron heating (ICH), and neutral beam injection (NBI) in the Large Helical Device (LHD) at Toki, Japan. The ion temperature at the plasma center is measured by a crystal spectrometer with a charge-coupled device (CCD) detector observing Doppler broadening of X-ray lines of He-like Ti XXI and Ar XVII [1]. Successful ion heating was found in ion cyclotron resonant frequency (ICRF) discharges (H minority, He majority), although the ion heating was not sufficient in H_2 and He NBI discharges [2].

LHD is equipped with a negative-ion-based NBI system, which consists of three tangential injectors. The hydrogen beam injection energy is as high as 150–180 keV. This choice attains good central power deposition even for relatively high-density plasmas of $(3–4) \times 10^{13} \mathrm{cm}^{-3}$, which yields high $n\tau T$. In low-density hydrogen plasmas, however, a large part of the injected beam passes through the plasma without ionization. Moreover, most of the ionized beam power is deposited to bulk electrons (P_e/P_{in} ~ 80%) because of the higher ratio of beam energy to electron temperature, E_{NBI}/T_e ~ 50. Therefore, it is quite difficult to increase the ion temperature in such discharges. The central ion temperature $T_i(0)$ increase generally saturates at less than 2.5 keV [2].

In the fifth experimental campaign in September 2001–February 2002, neon gas was introduced to increase the NBI absorption (ionization) power P_{abs} and the direct ion heating power P_i and to reduce the ion density n_i in low-density discharges. The ratio of P_i/n_i could be increased roughly 5 times in these neon discharges. An ion temperature up to 5 keV was successfully obtained with NBI power of 8 MW, and a linear relation was also found between the $T_i(0)$ and P_i/n_i [3,4], although the hydrogen coming into the discharge from the walls could not be sufficiently reduced.

The sixth experimental campaign began in September 2002 and ended on 7 February 2003. In order to obtain a further increase of the ion temperature, the hydrogen flux had to be reduced to a lower level. To achieve this, neon was used for glow discharge cleaning instead of hydrogen and helium. The neon glow discharge was carried out for 8 hours overnight (7 pm–3 am) followed by daily experiments on the days of 4–6 February. The neon glow discharge effectively displaced the recycling background ions from hydrogen to neon. As a result, the ion temperature increased day by day during the three experimental days. The effect of using a neon glow discharge for ion density control is now analyzed.

The second new experimental technique in the sixth experimental campaign was the use of an argon gas puff instead of neon, although this situation unfortunately makes the ion density analysis more complicated. Of course a reduction of the ion density was expected for the same electron density. A typical result is shown in Fig. 1. Densities for the horizontal axis are taken at the peak value after the argon gas puff in order to suggest the supplied argon ion density.

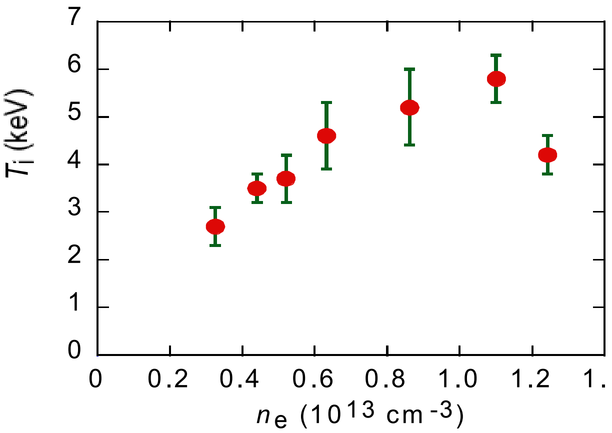

Fig.1. Central ion temperature as a function of line-averaged electron density after Ar gas puffing. The density is taken at the peak value, which typically reflects the quantity of the Ar puff.

The ion temperature is given by the peak value during discharge. The peak value of the ion temperature is normally obtained during the density decay phase after the argon gas puff. These data were taken on the first day in the three-day series of experiments. The highest ion temperature is found at $n_e \sim 1 \times 10^{13} \mathrm{cm}^{-3}$. At electron densities higher than $1 \times 10^{13} \mathrm{cm}^{-3}$, the plasma was shrunk by the argon radiation.

The highest ion temperature, $T_i(0) = 7$ keV, was obtained in the $R_{ax} = 3.60$ m configuration on the third day. The experimental waveform is shown in Fig. 2. The discharge is initiated and heated by high-power NBI ($P_{in} = 10$ MW, $E_{NBI} = 160–170$ keV). The direction of B_t is inverted to increase the net absorption power at the plasma center. Then, beams 1 and 3 are injected in the co-direction and the beam 2 is injected in the counter-direction. A small amount of Ar gas is puffed at $t = 0.5$ s. The density increases from $0.1 \times 10^{13} \mathrm{cm}^{-3}$ to $0.3 \times 10^{13} \mathrm{cm}^{-3}$ after the Ar puff. P_{abs} rapidly increases (a consequence of the Ne discharge cleaning) and maintains a high level of 3 MW, although the density is so low.

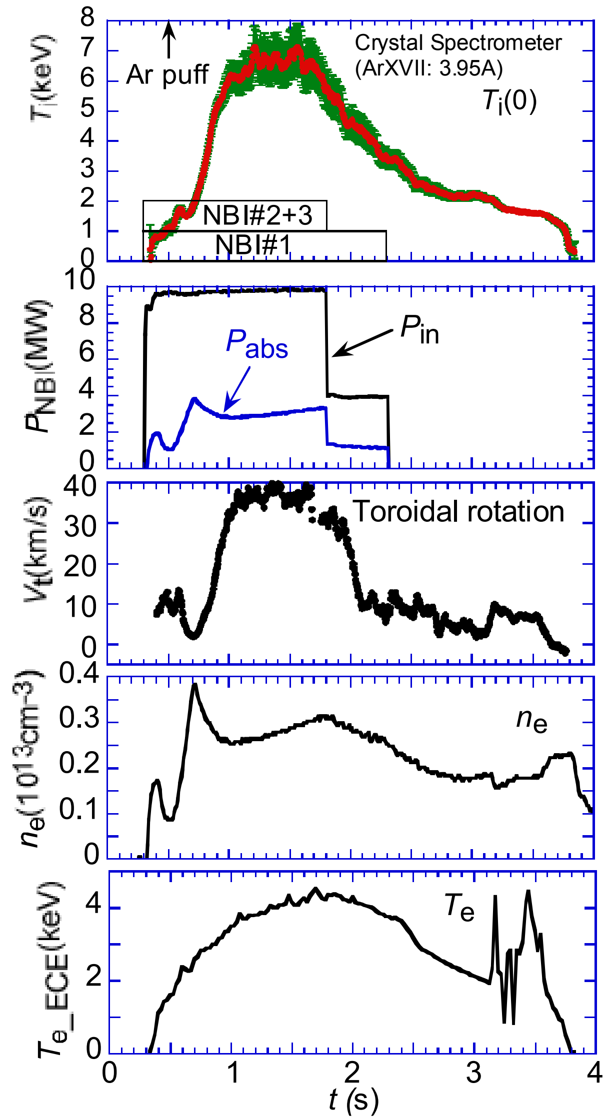

Fig. 2. Time evolution of ion temperature (T_i), NB I power (P_{in}: port-through power, P_{abs}: absorption power), toroidal rotation velocity (V_t), line-averaged electron density (n_e), and electron temperature (T_e) in Ar-seeded discharge with R_{ax} = 3.60 m configuration. The ion temperature is measured from a Doppler broadening of Ar XVII.The green vertical lines indicate error bars of $T_i(0)$.

The highest ion temperature is obtained after the Ar puff. It reaches 7 keV at $n_e \sim 0.3 \times 10^{13}\,\mathrm{cm}^{-3}$ after 0.7 s of the Ar puff. This increase of the ion temperature might originate in the increase of P_i/n_i. One notable thing in this high-Z discharge is the toroidal rotation speed, V_t, which rises rapidly with the increase of ion temperature. It reaches 40 km/s, which corresponds to 30% of the Ar ion thermal velocity. In the H_2 and He discharges, V_t was <10 km/s. The V_t decreases at t = 1.7 s beams 2 and 3 turn off. At the time of this small drop in V_t, $T_i(0)$ also begins to decreases gradually. After the beams 2 and 3 turn off, V_t drops rapidly. Observations from a series of these experiments indicate that V_t seems to be correlated with P_i/n_i. $T_e(0)$ is measured with electron cyclotron emission (ECE) diagnostics, which show $T_e(0)$ = 4.3 keV. The ECH pulse is applied during t = 3.1–3.6 s. Then, the ECE signal is influenced by electric power leakage from the 82.7 and 168-GHz gyrotrons. Meanwhile, the H_α signal rapidly increases at t = 0.7 s. It coincides with the rapid drop of n_e. After the increase of the H_α signal the n_e gradually increases. The increase in n_e during t = 1.0–1.8 s probably comes from an enhancement of the hydrogen flux. At present, the origin of the drop of $T_i(0)$ during the NBI pulse at t = 1.7 s seems to be the increase of n_i.

The calculation of n_i is complicated as mentioned before. From a rough spectroscopic calculation, n_i is estimated to be $\sim 0.1 \times 10^{13}\,\mathrm{cm}^{-3}$. The main ion is still hydrogen, but n_e is determined by the Ar ions. Hydrogen is also supplied from the NBI beam itself (so-called "beam fueling"), and this determines an upper limit of the highest ion temperature in a low-density, high-Z discharge. The total amount of absorbed hydrogen ions from the three beam injectors is $1.2 \times 10^{20}\,\mathrm{s}^{-1}$. Taking into account a reasonable core particle confinement time of 0.1 s ($\tau_E \sim 0.3$ s), the hydrogen ion density from NBI becomes $0.04 \times 10^{13}\,\mathrm{cm}^{-3}$. This suggests that we still have a margin to achieve higher ion temperature discharges. Up to now no beam fueling effect has been observed. The slowing-down time τ_s of the fast NBI ions becomes 1–2 s in the discharge. The effect of the long slowing down time is seen by the plasma behavior (t = 2.3–3.8 s) after switching off the NBI pulse.

The Ar XVII Doppler-broadened spectra are shown in Fig. 3. The data are taken at t = 0.440 s and 1.210 s of the Ar-seeded NBI discharge in Fig. 1. The spectra are processed with a time interval of 5 ms. The data are normally summed over 20 frames for the graph display, which results in a time resolution of 100 ms. The difference in ion temperature for argon and hydrogen is estimated to be smaller than a few hundreds of electron volts, taking into account the collisionality of beam–Ar and Ar–hydrogen.

The value of P_{abs} is estimated from the shine-through power, measured with a calorimeter, and the ratio of P_{abs} to P_{in}, is shown in Fig. 4 for Ar-, Ne- and H_2-puffed discharges. In the Ar- and Ne-puffed plasmas, P_{abs} is much greater than in the H_2 discharge, and it becomes 1.7 times at $n_e \sim 0.3 \times 10^{13}\,\mathrm{cm}^{-3}$. The ratio of P_{abs}/P_{in} can be fitted by $1 - \exp(\sigma n l)$, where σ represents the effective ionization cross section for the injected neutral beam. Because σ is proportional to Z_{eff} in plasmas, σ_{Ar} becomes nearly twice σ_H, and the Z_{eff} in the Ar-puffed discharge can be roughly estimated to be 6–8. Therefore, the ion density estimated from this method seems to be n_i/n_e = 1/2–1/3 in the Ar- and Ne-puffed discharges.

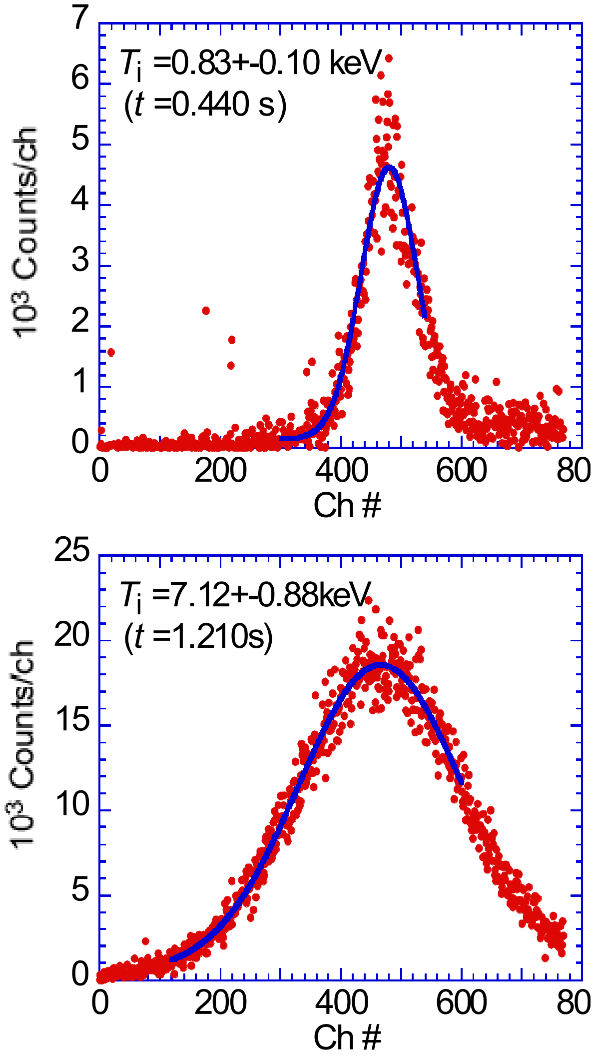

Fig. 3. He-like Ar XVII x-ray spectra (3.95 Å) showing Doppler broadening. Data are taken at t = 0.440 s and1.210 s from the discharge in Fig.1.

Figure 5 shows $T_i(0)$ as a function of plasma absorption power normalized by line-averaged electron density in the Ar- and Ne-puffed discharges. The electron temperature at R=3.76 m measured with ECE is also plotted in the figure. The ion temperature seems to be proportional to P_{abs}/n_e, while the electron temperature tends to saturate at higher P_{abs}/n_e range.

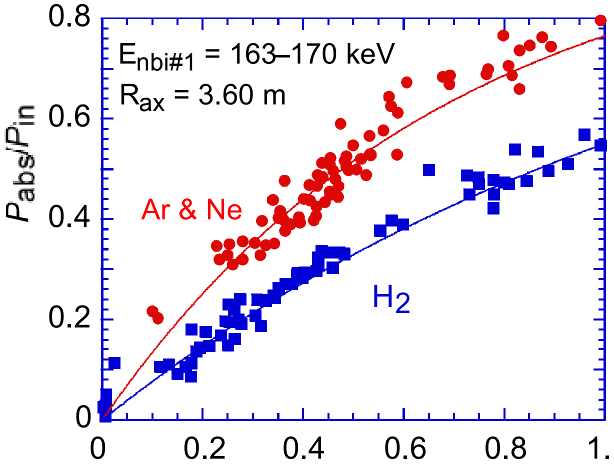

Fig. 4. Ratio of plasma absorption power (P_{abs}) to port-through power (P_{in}) of injected #1 neutral beam as a function of line-averaged electron density for Ar-, Ne- and H_2-puffed discharges (solid circles: Ar and Ne, solid squares: H_2).

Experiments were also done in the R_{ax} = 3.75 m configuration. A typical result is shown in Fig. 6. The operational scenario for the discharge is the same as the R_{ax} = 3.60 m case (see Fig. 2), and the Ar puff is supplied at t = 0.5 s. $T_i(0)$ reaches 6 keV and stays at the high temperature until the end of the NBI pulse. The data were taken on the second experimental day. If this experiment had been carried out on the third day, we would expect the same $T_i(0)$ as for the R_{ax} = 3.60 m case might be achieved. In comparison to the R_{ax} = 3.60 m configuration, the R_{ax} = 3.75 m configuration is known to have a relatively high effective helical ripple, which leads to a large neoclassical diffusion coefficient. The effective helical ripple $\varepsilon_{h\text{-}eff}$ in the R_{ax} = 3.75 m configuration is 2–3 times as large as in the R_{ax} = 3.60 m configuration, as shown in Table 1.

Table 1. A comparison of $\varepsilon_{h\text{-}eff}$ at 1/3 and 2/3 radii, for two different configurations.

	ρ = 1/3	ρ = 2/3
R_{ax} = 3.60 m	0.015	0.042
R_{ax} = 3.75 m	0.024	0.098

The obtained ion temperature is, roughly speaking, the same for both cases. In both discharges the hydrogen ion is in $1/\nu$ regime and the argon ion is in plateau regime. A transport calculation must be done to compare the two cases. A large toroidal rotation is also observed in this configuration. The relationship between V_t and $T_i(0)$ will be analyzed soon via an analysis of P_i and n_i.

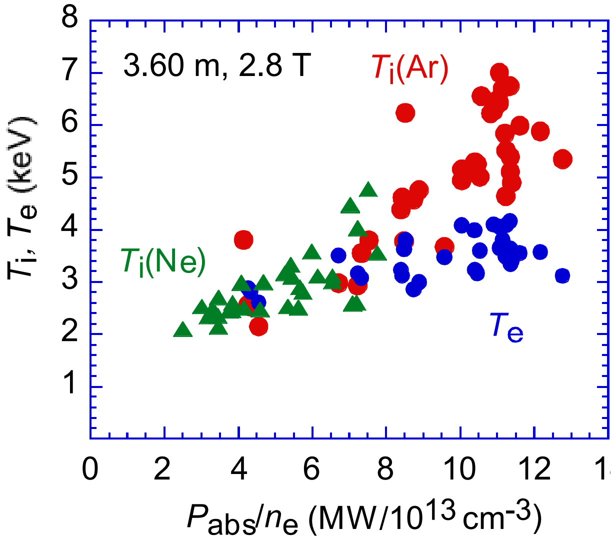

Fig. 5. Central ion temperature as a function of plasma absorption power normalized by line-averaged electron density for Ar- and Ne-puffed discharges. Electron temperature at R = 3.76 m is also plotted.

An impurity pellet injector was constructed [5] and installed in LHD last summer. Various kinds of spherical and cylindrical impurity pellets (C, Al, Ti, Mo) with a size of 0.5 –1.0 mm were injected into NBI discharges. A typical result for a cylindrical carbon pellet (1 mm dia. 1 mm long), performed on the third day of the experiment, is shown in Fig. 7. The carbon pellet was injected at t = 0.95 s in the R_{ax} = 3.60 m configuration. No gas puffing was carried out before injection. After the carbon injection, $T_i(0)$ gradually increases and reaches 5 keV. The lack of T_i data after the pellet injection is caused by a decrease in Ar XVII emission due to the sudden T_e drop.

A similar carbon pellet discharge, which had a similar high $T_i(0)$, was also obtained in the R_{ax} =3.75 m configuration with the exception of more rapid increase in the ion temperature—just 0.5 s between the start of injection and the time $T_i(0)$ reaches 5 keV. Generally the energy stored in the beam is high in NBI discharges of helical devices because of a high value of E_{NBI}/T_e. In low-density discharges especially, the value becomes very large, and the beam-ion slowing-down time becomes quite long. In this regime, the heat flux from the fast ions of NBI has a large influence on the pellet ablation [6]. To avoid ablating the pellet with the beam, the beams 2 and 3 are injected just after the pellet injection to avoid pellet ablation in the outer region of the plasma, and to achieve central particle deposition. This was a very effective means to increase the ion temperature. Density peaking was also observed. For impurity pellet injection, no clear difference in obtained $T_i(0)$ values was observed between the R_{ax} = 3.60 m and 3.75 m configurations. The $T_i(0)$ indicated a little increase for an Al pellet, and the plasma collapsed if 0.5-mm Ti or Mo pellets were used.

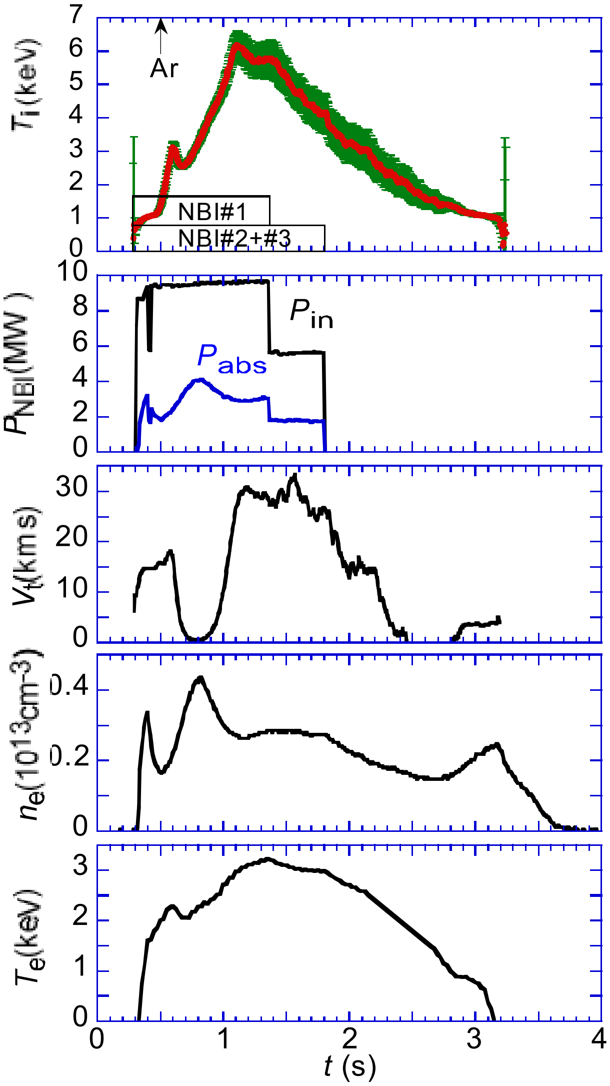

Fig. 6. Time evolution of ion temperature (T_i), NBI power (P_{in}: port-through power, P_{abs}: absorbed power), toroidal rotation velocity (V_t), line-averaged electron density (n_e), and electron temperature (T_e) in Ar-seeded discharge in the R_{ax} = 3.75 m configuration.

Finally, we expect that high-Z discharges will allow a good opportunity to study helical/toroidal ripple effects in LHD. This report is a bulletin and the description mentioned above is preliminary. Detailed analysis will be done soon.

One of the authors (SM) wishes to thank Dr. K. Y. Watanabe for helpful discussions.

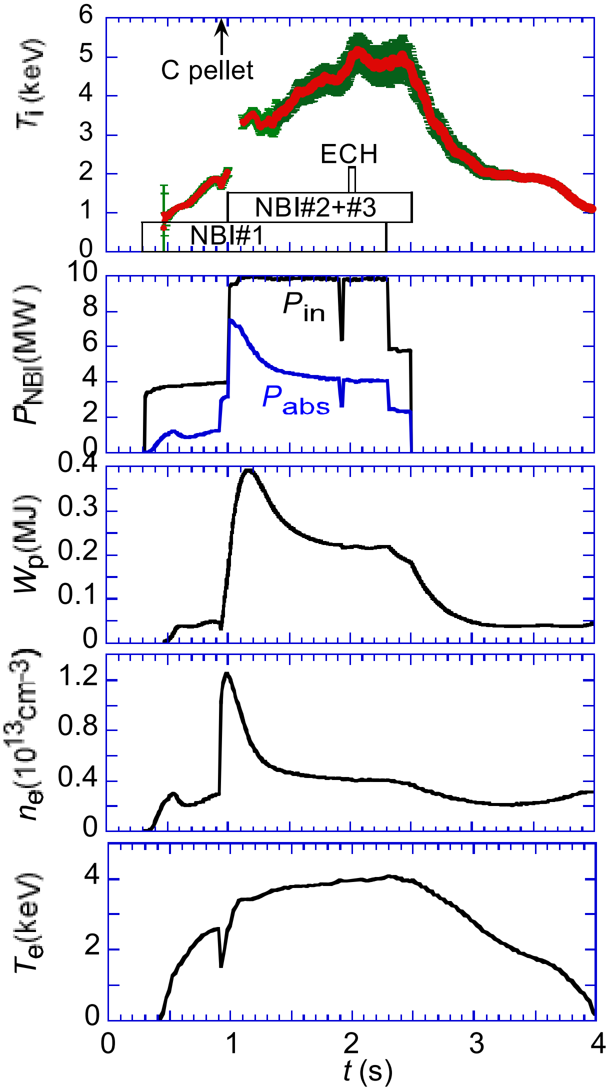

Fig. 7. Time evolution of ion temperature (T_i), NBI power (P_{in}: port-through power, P_{abs}: absorbed power), diamagnetic plasma stored energy (W_p), line-averaged electron density (n_e), and electron temperature (T_e) in Ar-seeded discharge with R_{ax} = 3.60 m configuration.

S. Morita and Y. Takeiri for the LHD Experimental Group
National Institute for Fusion Science
Toki 509-5292, Gifu, Japan

E-mail: morita@nifs.ac.jp and takeiri@nifs.ac.jp

References

[1] S. Morita and M. Goto, Rev. Sci. Instrum. **74**, (4) in press (2003).

[2] S. Morita et al., Nucl. Fusion **42** (2002) 1179.

[3] S. Morita et al., presented at the 19th IAEA Fusion Energy Conference, Lyon, 2002, EX/P2-18.

[4] Y. Takeiri et al., Phys. Plasmas **10** (5) in press (2003).

[5] H. Nozato et al., Rev. Sci. Instrum. **74** (3) in press (2003).

[6] S. Morita et al., Nucl. Fusion **42**, 876 (2002).

Extended abstracts

Two-dimensional correlation measurements of electron cyclotron emission fluctuations on the stellarator Wendelstein 7-AS

To appear in Rev. Sci. Instrum. **74**, March 2003.

The miniaturization of receiver arrays allows the arrangement of numerous poloidally staggered radial sight lines of an electron cyclotron emission (ECE) diagnostic for the measurement of the electron temperature and its fluctuations. Such an array can make possible two-dimensional (2-D) imaging of the electron temperature and its fluctuations caused by plasma turbulence. For the stellarator W7-AS, a fully monolithic microwave integrated circuit 150-GHz subharmonic mixer array is under development.

As a first step, a 2-D ECE system for the measurement of electron temperature fluctuations using four individual horn-reflector arrangements (see Fig. 1) in conjunction with multichannel heterodyne radiometers was installed and set into operation. With Gaussian beam optics and four poloidally staggered sight lines, electron temperature fluctuations could be characterized in the radial and poloidal directions simultaneously. First observations in purely electron cyclotron resonance heated stellarator plasmas reveal a broadband drift-wave feature. Earlier experiments, showing a decrease of the electron temperature fluctuation level with increasing heating power, were confirmed. Additionally it was revealed using the 2-D ECE correlation radiometer that an increased velocity shear might account for the decrease of the coherence length and thus for the reduction of the electron temperature fluctuation level.

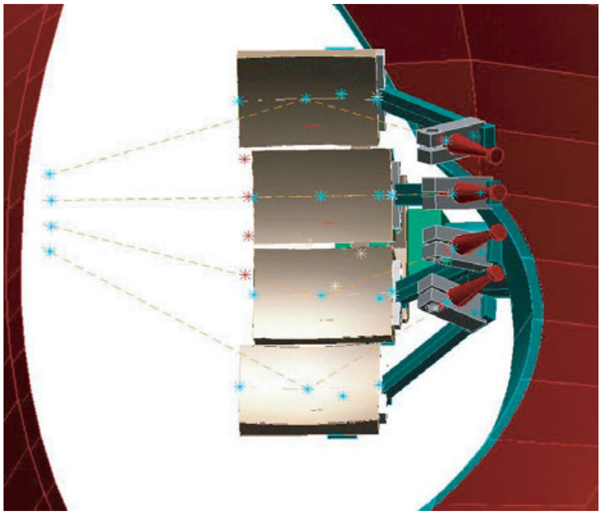

Fig. 1. Sketch of the four individual horn-reflector arrangements installed at W7-AS. The detection volumes are located on the high-field side of the plasma.

S. Bäumel, G. Michel, H. J. Hartfuß
Max-Planck-Institut für Plasmaphysik,
EURATOM Association, Wendelsteinstrasse 1, 17491
Greifswald, Germany

M. Rodriguèz-Girones Arboli, H. L. Hartnagel
Institut für Hochfrequenztechnik, Merckstrasse 25, 64283
Darmstadt, Germany

E-mail: baeumel@ipp.mpg.de

Resonant influence of helicity on Alfvén heating of plasma in stellarators

Plasma Phys. Controlled Fusion **45** (2), 121–132 (2003), online at stacks.iop.org/PPCF/45/121.

The distribution of antenna-driven fields of electromagnetic waves in the local Alfvén resonance (AR) region is studied under the resonant conditions, when the axial period of the fundamental harmonics of magneto-hydrodynamic oscillations in the axial direction is twice as large as the pitch length, and the poloidal number of the fundamental harmonics is twice as small as the polarity of the helical coils. It is shown that taking into account the helical inhomogeneity of the steady magnetic field can the remove infinite discontinuity of the wave fields, which is present in the case of straight confining magnetic field, rather than using the electron inertia or finite ion Larmor radius. Radio-frequency (RF) power absorption within the local AR is compared with the case when the AR structure is governed by electron inertia or finite ion Larmor radius. Another approach is proposed to explain the helicity-induced gap in the Alfvén continuum.

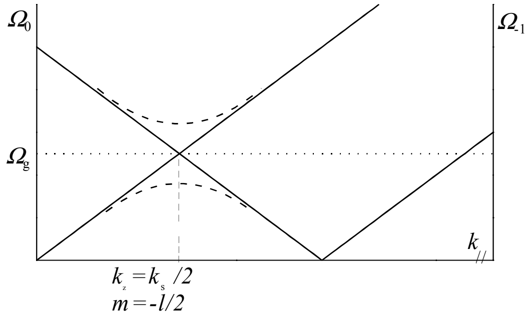

Fig. 2. Schematic description of the local Alfvén resonance frequency dependence upon parallel wave vector. Solid lines correspond to the case of the unperturbed magnetic field. Dashed lines demonstrate the helicity induced gap in the spectrum, caused by helical magnetic field. The dotted line corresponds to the frequency of the generator.

I. O.Girka,[1] V. I. Lapshin,[1] R. Schneider[2]
1. Kharkiv National University, Svobody Sq. 4
Kharkiv, 61077, Ukraine
2. Max-Planck Institut für Plasmaphysik, Teilinstitut Greifswald,
Wendelsteinstrasse, 1
Greifswald, D-17491, Germany